Adaptive time-delay estimation and control of optimized Stewart robot

Tajdari, F.

DOI
10.1177/10775463221137141

Publication date
2022

Document Version
Final published version

Published in
Journal of Vibration and Control

Citation (APA)
Tajdari, F. (2022). Adaptive time-delay estimation and control of optimized Stewart robot. *Journal of Vibration and Control*, *29*(23-24), 5511-5531. https://doi.org/10.1177/10775463221137141

Original Manuscript

Journal of Vibration and Control
2022, Vol. 0(0) 1–21

DOI: 10.1177/10775463221137141
journals.sagepub.com/home/jvc

Adaptive time-delay estimation and control of optimized Stewart robot

Farzam Tajdari

Abstract

Aiming at a more efficient and accurate performance of parallel manipulators in the existence of complex kinematics and dynamics, a robust generalizable methodology is proposed here for an integrated 6-DOF Stewart platform with rotary time-delayed actuators torque control. The suggested method employs a time-delay linear–quadratic integral regulator with online artificial neural network gain adjustment. The unknown time-delay is estimated through a novel robust adaptive estimator. The global asymptotic stability of the estimator is proved via a Lyapunov function. The controller is developed in MATLAB software and implemented on the robot designed in ADAMS software to ensure that the real-time tracking error of a nonlinear system with an unknown time-delay is kept to a minimum. The sensitivity of the controller to the parameter choices is studied via implementing the controller in ADAMS software and is validated by investigating the performance on a naturalistic fabricated robot. The approach is assessed using simulation and experimental tests to show the feasibility, optimum, and zero-error convergence of the technique developed.

Keywords

time-delay actuator, adaptive estimator, torque control, robust control, artificial neural network

1. Introduction

Parallel mechanisms over serial manipulators are alternatively suggested in applications such as surgeries (Orekhov et al., 2016; Saeedi-Hosseiny et al., 2021; Tajdari et al., 2020b) and scanning (Huang et al., 2018; Lee et al., 2022) which require higher acceleration and speed, better accuracy, and lighter weight (Taghirad, 2013). In particular, the highly precise scans of the human body for surgeries, the creation of anatomically adaptable rehabilitation devices (Nomura et al., 2016), and the next generation of Ultra Personalized Products and Services (UPPS) (Minnoye et al., 2022) attract more interest according to the necessity of robot-influenced health and human survival. One challenging scanning scenario as the implementation candidate for this study is rapid automatic breast scanning (Sun et al., 2018), although it is a very complex operation due to the flexibility and deformability of the breast tissue, particularly in motion scanning. The high accuracy requires a clear understanding of the control of such parallel robots that investigate complex dynamic, sophisticated control approaches (Shoham et al., 2003), and implementation objections such as a sensor or actuator time-delays (Jin et al., 2017).

The key goal of parallel robot control design is to achieve an exact continuation of the target direction and orientation of dynamic or static variables in the robot's moving end-effector (Merlet, 2006). While multiple control systems (Ju et al., 2022), such as optimal feedback robotics control (Tourajizadeh et al., 2016), monitoring backstage adaptive control (Huang and Fu, 2004), sliding mode (SM) (Zhu et al., 2022; Tajdari et al., 2017a), model predictive control (Hu et al., 2022), and PID controllers (Velasco et al., 2020), are available, fewer control procedures are utilized for Stewart robots with rotary actuators because of the extra complexity of the robot's dynamics. The reverse dynamic control methods are especially important for controlling the motion of the end-effector directly through the manipulators. The rotary robot torque control, which is an opening for further application of identification techniques, nonlinear control methods, and impedance manipulator control, is explored in limited studies (Yang et al., 2019).

Moreover, among the state-of-the-art studies that addressed the control of the rotary Stewart robot, few of them investigated the time-delay as an undeniable part of such

Faculty of Industrial Design Engineering, TUDelft, Delft, Netherlands

Received: 20 June 2022; accepted: 18 October 2022

Corresponding author:
Farzam Tajdari, Faculty of Industrial Design Engineering, Delft University of Technology, Landbergstraat 15, Delft 2628 CE, Netherlands.
Email: f.tajdari@tudelft.nl

robots emphasizing high accuracy. Time-delay control (TDC) is often an efficient way of tackling the issues listed above. The TDC scheme is widely utilized for significant applications, such as robot manipulators (Baek et al., 2021), underwater vehicles (Qi and Cai, 2021), and robots with flexibilities (Xu and Xu, 2022). Meanwhile, the use of time-delayed control commands will necessarily profit estimation errors, that is, time-delay estimation (TDE) errors, in practical control methodologies implementations.

In presence of high uncertainties and nonlinearities, for example, saturation, the TDE errors will be increased which causes instability of the closed-loop control system. Thus, the TDC approach is mainly employed as a general solution that benefits from its model-free feature. Additional robust control strategies, such as SM control (Li and Chen, 2018), terminal SM control (TSM) (Fu et al., 2022), and adaptive robust control (Ma et al., 2018), are now also being employed to ensure high precision and robustness. Because of the model-free TDE approach and the employed robust control techniques, TDE-based control schemes may provide great control efficiency straightforwardly. The bulk of current TDE-based control schemes, on the other hand, is strictly confined to constant control gain, ensuring that fixed gain is always utilized. However, time-varying dynamic disruptions usually occur in practical implementations, which may result in the control output degrading. As previously mentioned (Wang et al., 2018a), control precision is roughly proportional to control of the gain. With a greater control gain, better control precision and faster dynamical reaction are feasible. Moreover, there will be a significant noise effect, as well as control device instability, when an inappropriately high control gain is used. Similarly, when the control gain is set too low, the control scheme degrades and may even fail to track the desired trajectory. Because control tasks and requirements for parallel manipulators vary with time, maintaining adequate detailed control output under complicated situations while utilizing a fixed control gain is typically quite challenging. As a result, adaptive TDC (ATDC) methods with self-tuning power gain have been suggested and investigated to solve the aforementioned concerns (Baek et al., 2017; Tajdari and Toulkani, 2021). However, it is challenging to utilize in real applications due to its inherent noise susceptibility and the usage of many control settings. As a result, the built algorithm was only demonstrated using simulations with a single degree of freedom (DOF). Then, for the control gain (Baek et al., 2017), an auto-tuning algorithm was developed. Although the ATDC systems discussed above have produced intriguing theoretical and experimental findings, the disadvantages are several (Wang et al., 2018b): First, the adaptive legislation that has been suggested cannot quickly and accurately reflect the tracking error (Jin et al., 2016), or might create significant chatters owing to the usage of the discontinuous function, and second, the designed ATDC schemes (Baek et al., 2017) used traditional linear ATDC schemes.

This paper seeks to establish and test for the complex parallel structure of a novel robust torque control approach in presence of huge time-delay with the actuators to optimize torques and reduce tracking errors in order to resolve all the challenges listed above. Moreover, the controller is validated through a valid nonlinear test-bed through the ADAMS model proposed in Tajdari and Toulkani (2021) and assessed experimentally via a fabricated robot. In Tajdari et al. (2020a) and Tajdari and Toulkani (2021), a robust optimal torque controller for the same Stewart platform is discussed; however, the works did not investigate the impact of time-delay on the performance of the robot and also optimal design of the platform which are extensively studied in this paper. In addition, an introductory version of this study is presented in Tajdari et al. (2021), which is collaborated here with optimal design of the robot dynamic; architecting of a robust estimator for the time-varying time-delay; a more rigorous concept; a comprehensive verification on the stability of controller parameters for the proposed control law; studying on the degree of robustness regarding parameter selection via numerical experiments; and extra numerical experiments, including a scenario grants a state-of-the-art regular control method and a scenario, which contains extra disturbances via the fabricated robot.

2. Equation of motion

2.1. Kinematics equation

The torques manipulated with motors and their rotational angles are the variables capable to be controlled in a Stewart platform that is actuated with rotary motors. A relationship between the variables of the motors and the location of the end-effector is reported as follows

$$\overline{L} = f\left(\overline{X}\right),\ \theta_M = g\left(\overline{L}\right), \tag{1}$$

where the end-effector's variables are presented as $\overline{X} = [\,\phi \quad \theta \quad \psi \quad x \quad y \quad z\,]^T$, where the rotation angles include ϕ, ψ, and θ of the end-effector about the X, Y, and Z axis, respectively, and the locations of the end-effector center of mass are defined as x, y, and z according to the fixed coordinate XYZ, presented in Figure 1(a). In addition, the $\overline{L} = [\,L_1 \quad L_2 \quad L_3 \quad L_4 \quad L_5 \quad L_6\,]^T$ addresses the distance from the joints on the fixed base $(\overrightarrow{P_i})$ to the corresponded joints on the end-effector $(\overrightarrow{p_i})$. Finally, $\theta_M = [\,\theta_{M_1} \quad \theta_{M_2} \quad \theta_{M_3} \quad \theta_{M_4} \quad \theta_{M_5} \quad \theta_{M_6}\,]^T$ represents the motor angular depicted in Figure 1(a). To reveal the connection between L_i and θ_{M_i}, the results of the same model in Tajdari et al. (2020a) are extracted from Van Nguyen and Ha (2018); Szufnarowski (2013); then

$$\theta_{M_i} = -\left(asind\left(\frac{\mathcal{C}_i}{\sqrt{\mathcal{A}_i^2+\mathcal{B}_i^2}}\right) - acosd\left(\frac{\mathcal{B}_i}{\sqrt{\mathcal{A}_i^2+\mathcal{B}_i^2}}\right) + 180\right) \tag{2}$$

where $\mathcal{A}_i, \mathcal{B}_i, \mathcal{C}_i \in U(\overline{X})$ and

$$\begin{aligned} \mathcal{A}_i &= 2\left|\overrightarrow{u}_i\right|\left(\left|\overrightarrow{L}_{i_x}\right|Sin(\theta_h) - \left|\overrightarrow{L}_{i_y}\right|Cos(\theta_h)\right), \\ \mathcal{B}_i &= 2\left|\overrightarrow{u}_i\right|\Big(\left|\overrightarrow{L}_{i_x}\right|Cos(\beta)Cos(\theta_h) \\ &\quad + \left|\overrightarrow{L}_{i_y}\right|Cos(\beta)Sin(\theta_h) - \left|\overrightarrow{L}_{i_z}\right|Sin(\beta)\Big) \\ \mathcal{C}_i &= \left|\overrightarrow{l}_i\right|^2 - \left|\overrightarrow{L}_i\right|^2 \end{aligned} \tag{3}$$

where θ_h defines the angle between $\overrightarrow{P}_i$ and $\overrightarrow{X}$ in the XYZ axis, and β is the motor installation angle to the horizon. The defined formula in (2) explains that measuring the $\overline{X}$ via a sensor mounted on the end-effector results in determining the corresponding operating angle value of each motor, which is useful to practically implement position controller approaches on such robots.

2.2. Kinetics equations

Here, employing the Newton–Euler method, the dynamic formulation of the Stewart platform equipped with six rotary motors is concluded from Van Nguyen and Ha (2018); Szufnarowski (2013). The platform includes, as shown in Figure 1, a moving plate as the end-effector, a sedentary plate as the base, six rotary actuators as manipulators to move the end-effector, and six legs connected to their corresponded motors. The spherical joints are utilized to carry the end-effector and the backbone to the six legs.

The formulation extraction is summarized to introduce the different complex properties of the structures and outcomes. The analyzed Stewart platform is drawn in Figure 1(a). The kinetics formulations regarding the end-effector are extracted as

$$\Sigma\overrightarrow{M} = \overline{I}\,\overrightarrow{\alpha} \tag{4}$$

$$\Sigma\overrightarrow{F} = \overline{m}\,\overrightarrow{a} \tag{5}$$

where $\overrightarrow{\alpha}$ defines the vector of the angular acceleration, and $\overrightarrow{a}$ determines the vector of the linear acceleration of the end-effector's center of mass. Furthermore, matrix $\overline{m}$ consists of the mass value (m) of the end-effector, and matrix $\overline{I}$ contains the end-effector moment of inertia around x, y, and z axes; then

$$\begin{bmatrix} \overline{I} & 0_{3\times3} \\ 0_{3\times3} & \overline{m} \end{bmatrix} \ddot{X} = \begin{bmatrix} M \\ F \end{bmatrix} \tag{6}$$

where

$$\overline{I} = diag\left(I_{xx}, I_{yy}, I_{zz}\right),\ \overline{m} = diag(m, m, m) \tag{7}$$

$$M = \left[M_x, M_y, M_z\right]^T, F = \left[F_x, F_y, F_z\right]^T, \tag{8}$$

where M and F, depicted in Figure 1(a), explain all the torques and the forces applied to the end-effector, respectively. Referring the manipulated torques control, the dynamic equations are extracted as a controllable variable–torque relationship as follows

$$\begin{bmatrix} \overline{I} & 0_{3\times3} \\ 0_{3\times3} & \overline{m} \end{bmatrix} \ddot{\overline{X}} = \begin{bmatrix} M \\ F \end{bmatrix} = \tau_{6\times6} T \tag{9}$$

where $T = [\,T_1 \quad T_2 \quad T_3 \quad T_4 \quad T_5 \quad T_6\,]^T$, and each of the T_i is representing the manipulated torque by its corresponded i^{th} motor. In more detail, the kinetics

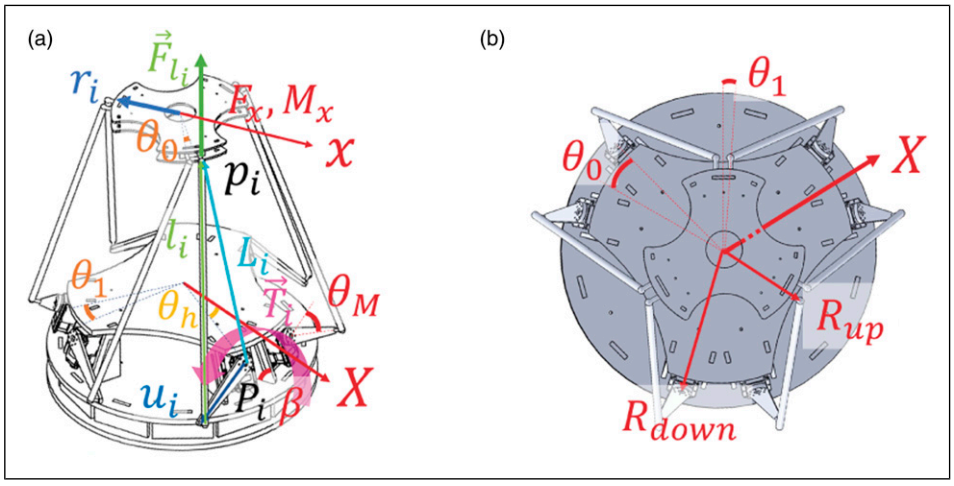

Figure 1. The Stewart platform mechanism: (a) defined variables and vectors and (b) the top view of the designed Stewart platform in SolidWorks software.

equations are formulated employing their unit vectors as explained in (10)

$$\Sigma\vec{M} = \Sigma\vec{r}_i \times \vec{F}_{l_i} = \Sigma\vec{p}_i \times \vec{e}_{l_i}\left|\vec{F}_{l_i}\right| = \Sigma\vec{e}_{M_i}\left|\vec{F}_{l_i}\right| \quad (10)$$

in which $\vec{e}_{M_i} = \vec{p}_i \times \vec{e}_{l_i}$ (i.e., $\vec{e}$ determines the unit vector of its corresponding vector). Then

$$\Sigma\vec{F} = \Sigma\vec{e_{l_i}}\left|\vec{F_{l_i}}\right| \quad (11)$$

thus

$$\begin{bmatrix} M \\ F \end{bmatrix} = \begin{bmatrix} e_{M_1} & \cdots & e_{M_6} \\ e_{l_1} & \cdots & e_{l_6} \end{bmatrix} \begin{bmatrix} F_{l_1} \\ \vdots \\ F_{l_6} \end{bmatrix} \quad (12)$$

where

$$\tau_1 = \begin{bmatrix} e_{M_1} & \cdots & e_{M_6} \\ e_{l_1} & \cdots & e_{l_6} \end{bmatrix}. \quad (13)$$

As $\vec{F}_{l_i} = \vec{e}_{l_i} \cdot \vec{e}_{N_i}\left|\vec{T}_i\right| \Big/ \left|\vec{u}_i\right|$, where $\vec{e}_{N_i}$ is the unit vector of $\vec{T}_i$, then

$$\begin{bmatrix} F_{l_1} \\ \vdots \\ F_{l_6} \end{bmatrix} = \begin{bmatrix} \dfrac{\vec{e}_{l_1} \cdot \vec{e}_{N_1}}{\left|\vec{u}_1\right|} & \cdots & 0 \\ \vdots & \ddots & \vdots \\ 0 & \cdots & \dfrac{\vec{e}_{l_6} \cdot \vec{e}_{N_6}}{\left|\vec{u}_6\right|} \end{bmatrix} \begin{bmatrix} T_1 \\ \vdots \\ T_6 \end{bmatrix}. \quad (14)$$

Considering

$$\tau_2 = \begin{bmatrix} \dfrac{\vec{e}_{l_1} \cdot \vec{e}_{N_1}}{\left|\vec{u}_1\right|} & \cdots & 0 \\ \vdots & \ddots & \vdots \\ 0 & \cdots & \dfrac{\vec{e}_{l_6} \cdot \vec{e}_{N_6}}{\left|\vec{u}_6\right|} \end{bmatrix} \quad (15)$$

and

$$\begin{bmatrix} \overline{I} & 0_{3\times3} \\ 0_{3\times3} & \overline{m} \end{bmatrix} \ddot{\overline{X}} = \begin{bmatrix} M \\ F \end{bmatrix} = \tau_{6\times6} T = \tau_1 \tau_2 T \quad (16)$$

Hence, the final dynamic transfer matrix explains the torque–force relationship on the end-effector based on the motor torques is $\tau = \tau_1\tau_2$, which leads us to directly apply the torque control methods as follows

$$\ddot{\overline{X}} = \tau_{tot} T \quad (17)$$

where

$$\tau_{tot} = \begin{bmatrix} \overline{I} & 0_{3\times3} \\ 0_{3\times3} & \overline{m} \end{bmatrix}^{-1} \tau. \quad (18)$$

2.3. Optimal design of the dynamic robot platform

In order to establish the optimal kinematic and dynamic performance of the robot, a number of simplified assumptions were considered, and the rest of the parameters are optimally designed based on the desired work-space of the end-effector including dynamic and static features. As the future application of the robot is collaborating to carry a breast scanner mentioned in the Introduction section, the dimensions of end-effector and base of the robot are considered predefined. According to Figure 1(a) and Figure 1(b), the assumed parameters are summarized in Table 1(a), and u_i and l_i are optimized through the following cost function

$$J_{tot} = \begin{cases} Minimizing: & J_L, J_T \\ Maximizing: & J_{WS}, J_u, J_l \end{cases} \quad (19)$$

where J_{tot} is the total cost function that includes both minimization and maximization terms. Regarding the minimization, J_L consists of the length of each element of $\overline{L}$ formulated as

$$J_L = \sum_{i=1}^{6} |L_i|^2 \quad (20)$$

As the desired work-space is predefined, J_L explains the minimum possible dimension that covers the work-space. Continuously, J_T denotes the maximum possible torque on each motor. Considering $\overline{X}$ is periodically changing with frequency of 6 Hz (6 times more than the practical frequency used in the Results section), then $\ddot{\overline{X}} = -36\overline{X}$, and from (17), we will have

$$J_T = \left|\tau_{tot}^{-1}\left(-36\overline{X}\right)\right|^2 \quad (21)$$

Regarding the maximization, the moving links' cost functions are assumed as below

$$J_u = \sum_{i=1}^{6} |u_i|^2 \quad (22)$$

$$J_l = \sum_{i=1}^{6} |l_i|^2. \quad (23)$$

Continuously, J_{WS} belongs to the maximum work-space and is explained as follows

Table 1. The parameters and assumptions used for the robot's dimension.

(a) The choice of options

Parameter	Value	Description
R_{up}	0.12 (m)	Norm p_i
R_{down}	0.22 (m)	Norm P_i
θ_0	5°	Angle joint on base
θ_1	15°	Angle joint on end-effector
β	70°	The motor installing angle

(b) Optimal parameter results

	Constraint	
Parameter	$z-z_0 \le 0$	$z_0-z \le 0$
u_i (m)	0.065	0.108
l_i (m)	0.363	0.404

(c) Dynamical features of Stewart platform's components

Component	Dimension (m)	Inertia [I_x, I_y, I_z] (× 10^{-4} kg.m^2)	Mass (kg)	Quantity
l_i	0.404	[16, 16, 0.01]	0.08	6
u_i	0.11	[0.01, 0.58, 0.6]	0.04	6
End-effector	Circle (R_{up} = 0.12)	[30, 30, 60]	4	1
Base	Circle (R_{down} = 0.22)	[270, 270, 540]	7	1

$$J_{WS} = \left\| \begin{bmatrix} \overline{X} - \overline{X}_0 \\ \theta_M - \theta_{M_0} \end{bmatrix} \right\|^2 \tag{24}$$

where $\overline{X}_0 = [0, 0, 0.38, 0, 0, 0,]^T$ and $\theta_{M_0} = [90°, 90°, 90°, 90°, 90°, 90°]^T$. Thus, the optimal problem is finding a set of optimal design parameters l_i and u_i such that

$$\min J_{tot} = J_L + J_T - J_{WS} - J_u - J_l \tag{25}$$

subject to

$$-\frac{\pi}{6}(rad) \le \phi \le \frac{\pi}{6}(rad)$$
$$-\frac{\pi}{6}(rad) \le \theta \le \frac{\pi}{6}(rad)$$
$$-\frac{\pi}{6}(rad) \le \psi \le \frac{\pi}{6}(rad)$$
$$-0.08(m) \le x \le 0.08(m)$$
$$-0.08(m) \le y \le 0.08(m)$$
$$0.3(m) \le z \le 0.46(m)$$
$$0° \le \theta_{M_i} \le 180°$$
$$-1.5(N.m) \le T_i \le 1.5(N.m)$$
$$0.05(m) \le u_i \le 0.2(m)$$
$$0.1(m) \le l_i \le 0.6(m)$$

and with a conditional constraint of

$$\begin{cases} z - z_0 \le 0 & for\ lower\ boundary \\ z_0 - z \le 0 & for\ upper\ boundary \end{cases} \tag{26}$$

Two conditional constraints are proposed to lead the optimization process towards the farthest maximum point (z = 0.46 m) and farthest minimum point (z = 0.3 m) locations that the end-effector should travel from its initial location (z_0 = 0.38 m). By applying the algorithm in Lagarias et al. (1998) such as Tajdari et al. (2022a), the optimal parameters are designed, and for each of the constraints, the minimum values are obtained, as reported in Table 1(b). Thus, the maximum of the optimal values for each of the parameters is selected to make sure that both the constraint conditions are covered, and then u_i = 0.11(m) and l_i = 0.404(m).

2.4. Nonlinear model

In terms of controller assessment, it is necessary to prepare a realistic nonlinear model that can describe the actual robot. As certain dynamical constraints, for example, the collision of objects, stiffness, and elasticity of rigid bodies, and friction between hard surfaces, are not easy to be modeled in MATLAB software; an ADAMS model (Tajdari and Toulkani, 2021) is established based on the optimally designed dimensions in the Optimal Design of the Dynamic Robot Platform

section. Since the ability to encrypt and apply multiple control methods in ADAMS software is missing, the model is controlled online with MATLAB software. Second, the machine 3D model in the SolidWorks program is shown in Figure 1(b). Then, the 3D model can be imported into ADAMS and the aforementioned constraints in the Kinetics Equations section are applied to the model of the robot, such as joint sizes, materials, body densities, rigidity towards each other, and friction between hard surfaces. The parameters in Figure 1(b) and Figure 1(a) are explained in Table 1(a), and Table 1(c) reports the used dynamic parameters. According to the table, the platform includes 14 components of mass and moment of inertia.

3. Adaptive time-delay estimator design

We aim at designing a novel adaptive estimator to estimate the actuators' time-delay. To do so, the needed assumptions are presented, and then the integration of the method to the designed time-delay optimal controller is explained, and ultimately, the convergence of the estimated time-delay value and the method's global asymptotic stability are investigated. In total, by comparing the designed torque (T) and measured used torque (T_s) on the actuators, the estimator defines the exact value of the time-delay for each motor. Let us define the integral error states (E_μ)

$$E_\mu = \int T\left(t - \widehat{\mu}\Delta t\right) - T_s(t)\, dt, \tag{27}$$

where T_s naturally has an unknown delay with T, and $\widehat{\mu}$ is the estimated delayed steps between the 2 signals of T and T_s. Thus, the integral error system led to

$$\dot{E}_\mu = T\left(t - \widehat{\mu}\Delta t\right) - T_s(t), \tag{28}$$

which can be rewritten as

$$\dot{X} = B_e u_e + r_e, \tag{29}$$

where

$$X = \int T\left(t - \widehat{\mu}\Delta t\right) dt, \tag{30}$$

$$B_e = 1, r_e = T_s(t), \tag{31}$$

and u_e is the controllable variable to control the X and is assumed as a combination of X and r_e as follows

$$u_e = -\widehat{\mu}X + \widehat{\mu}r_e, \tag{32}$$

where $\widehat{\mu}$ is the unknown matrice of the time-delay value that should be estimated. Then, the system in (29) is controlled via model reference adaptive control (MRAC) (Slotine et al., 1991; Tajdari and Roncoli, 2021), which allows estimating the unknown parameters $\widehat{\mu}$ and minimize the tracking error simultaneously. By assuming $\tilde{a} = \begin{bmatrix} -\widehat{\mu} & \widehat{\mu} \end{bmatrix}$, the feedback control law is

$$u_e = \tilde{a}\begin{bmatrix} X \\ r_e \end{bmatrix}. \tag{33}$$

A model reference is considered as

$$\dot{X}_M = -A_M X_M + B_M r_e, \tag{34}$$

where pair (A_M, B_M) are optional matrices that establish a stable dynamic of the model reference. Considering the error between the integral states and the model reference as $e = X - X_M$, then

$$\begin{aligned} \dot{e} &= \dot{X} - \dot{X}_M \\ &= B_e\left(-\widehat{\mu}X + \widehat{\mu}r_e\right) + r_e + A_M X_M - B_M r_e + A_M X - A_M X \\ &= -A_M(X - X_M) + B_e\left(-\widehat{\mu} + \frac{A_M}{B_e}\right)X + B_e\left(\widehat{\mu} - \frac{B_M - I}{B_e}\right)r_e \\ &= -A_M e + B_e\left(-\widehat{\mu} + \frac{A_M}{B_e}\right)X + B_e\left(\widehat{\mu} - \frac{B_M - I}{B_e}\right)r_e, \end{aligned} \tag{35}$$

which is concluded to

$$\begin{aligned} e &= \frac{B_e}{sI + A_M}\begin{bmatrix} -\widehat{\mu} + \frac{A_M}{B_e} & \widehat{\mu} - \frac{B_M - I}{B_e} \end{bmatrix}\begin{bmatrix} X \\ r_e \end{bmatrix}, \\ &= \frac{|B_e|}{sI + A_M}\begin{bmatrix} -\widehat{\mu}\mathrm{Sn}(B_e) + \frac{A_M}{|B_e|} & \widehat{\mu}\mathrm{Sn}(B_e) - \frac{B_M - I}{|B_e|} \end{bmatrix}\begin{bmatrix} X \\ r_e \end{bmatrix}, \end{aligned} \tag{36}$$

where s represents the Laplace variable, I is the identity matrix, and Sn is the sign operator. The error dynamic of (36) remains stable by the time, as A_M was selected as a stable matrix (means A_M has negative eigenvalues), if $\tilde{a}$ is bounded or $\tilde{a}$ is converging (Tajdari and Roncoli, 2022). Please note that A_M and B_M are usually chosen as constant matrices. Then, to define the stability of the system, let's propose

$$u_e = \mathrm{Sn}(B_e)\tilde{a}\begin{bmatrix} X \\ r_e \end{bmatrix}, \tag{37}$$

To study the convergence of $\tilde{a}$, the Lyapunov function given below is proposed

$$\mathcal{V} = X^T \mathcal{P} X + \tilde{a}^T \Gamma^{-1} \tilde{a}, \tag{38}$$

where $\mathcal{P} \geq 0$ and $\Gamma > 0$ imply that $\mathcal{V} > 0$. For stability, it would be enough if $\dot{\mathcal{V}} \leq 0$ (Tajdari et al., 2022b), and then

$$\frac{d\mathcal{V}}{dt} = \dot{X}^T \mathcal{P} X + X^T \mathcal{P} \dot{X} + \dot{\tilde{a}}^T \Gamma^{-1} \tilde{a} + \tilde{a}^T \Gamma^{-1} \dot{\tilde{a}}. \quad (39)$$

By replacing $v = \begin{bmatrix} X \\ r_e \end{bmatrix}$ in (37), we obtain $u_e = \mathrm{Sn}(B_e) v^T \tilde{a}$; thus

$$\frac{d\mathcal{V}}{dt} = 2X^T \mathcal{P} B_e \, sign(B_e) v^T \tilde{a} + 2\dot{\tilde{a}}^T \Gamma^{-1} \tilde{a}. \quad (40)$$

If it is assumed that $\mathcal{P}B_e = C^T$, $e = X^T C^T$, and $d\mathcal{V}/dt = 0$, then (40) results in

$$-2\ \mathrm{Sn}(B_e) e v^T \tilde{a} = 2\dot{a}\Gamma^{-1}\tilde{a} \quad (41)$$

thus, to guarantee the stability and convergence of estimated values, the changes in the unknown parameters over time should follow the adaptation rule as

$$\dot{\tilde{a}} = -\Gamma \mathrm{Sn}(B_e) e v^T. \quad (42)$$

To implement the parameter estimation in a discrete form, it is considered that $\dot{\tilde{a}}(k) = (\tilde{a}(k) - \tilde{a}(k-1))/\Delta t$, and then the adaptation rule in (42) would be

$$\tilde{a}(k) = \tilde{a}(k-1) - \Delta t\left(\Gamma\, \mathrm{Sn}(B_e) e v^T\right) \quad (43)$$

Based on our observations, when $|\dot{\tilde{a}}| > 1$, the estimated values of $\tilde{a}$ are highly fluctuating which results in a deterioration of the estimator performance. To prohibit this, the Γ called growth ratio is designed as follows to keep $\Gamma \leq 1$ and to guarantee a smooth convergence

$$\Gamma(k) = \begin{cases} \dfrac{1}{\left|\dot{\tilde{a}}(k)\right|^{v_1}}, \text{if} \left|\dot{\tilde{a}}(k)\right| > 1, \\ \left|\dot{\tilde{a}}(k)\right|^{v_2}, \text{if} \left|\dot{\tilde{a}}(k)\right| \leq 1. \end{cases} \quad (44)$$

Moreover, as the estimated number of delayed iterations should be an integer value, the implemented number of delayed iterations as μ is considered as follows

$$\mu = floor\left(\widehat{\mu} + 0.5\right). \quad (45)$$

4. Discussion

A value of 0.5 is added to $\widehat{\mu}$ to avoid fluctuation of μ around an integer value with a deviation less than 0.5 which establishes a region of attraction with a length of 1 around the integer value.

In (44), v_1 and v_2 are very effective to the changes of Γ by the time. And, the huge parameters of Γ can lead the system to an unstable condition as the system and control scheme is very dependent on the estimated time-delay. Thus, Γ should be chosen so that the estimator is fast enough with the least overshoot. For the possible domain of v_1 and v_2, four conditions exist according to (44) as follows.

1. $v_1 < 0$ and $v_2 < 0$: Which is unstable as Γ would be very big number; thus, we have overshoots.
2. $v_1 < 0$ and $v_2 > 0$: For some cases that $|\dot{\tilde{a}}(k)| > 1$, Γ would be very huge resulting in instability.
3. $v_1 \geq 0$ and $v_2 \geq 0$: Some stable points may be found here as with this condition, Γ is bounded.
4. $v_1 > 0$ and $v_2 < 0$: For small values of $|\dot{\tilde{a}}(k)|$, Γ would be very huge which is more probable to happen than condition 2.

Accordingly, in this study, the proper values of v_1 and v_2 are investigated in condition 3, as they will be explained in the Sensitivity Analysis section.

5. Controller design

Because the developed dynamic platform in the ADAMS software in Tajdari and Toulkani (2021) consists of the nonlinear parameters of the actual platform, this is accurately a nonlinear Stewart system, and the proposed controller must be able to penalize tracking errors in the presence of nonlinearities to monitor those systems (Åström and Hägglund, 1995). In addition to the robustness, parallel manipulator input signals optimization is a problem to be tackled during the control design process. Therefore, an optimal control scheme for the linear–quadratic integral (LQI) is an appropriate choice for the nonlinear control problem.

5.1. State-space equations

The state-space and dynamic equations of the Stewart robot can be established as below

$$\dot{\bar{x}}(t) = \overline{A}_c \bar{x}(t) + \overline{B}_c(t) T(t) + \overline{d}_c(t) \quad (46)$$

where $\bar{x}$ consists of the main states in $\overline{X}$ and the speed of the states with size $N \times 1$ (where $N = 2n$). Consequently, the dynamic of error can be defined as

$$\dot{\bar{e}}(t) = \overline{A}_c \bar{e}(t) + \overline{B}_c(t) T(t) + \overline{d}_c(t). \quad (47)$$

Accordingly, vector $\overline{d}_c$ represents the time-variant disturbance. $\bar{e}$ belongs to the error of the states and is proposed as $\bar{e} = \bar{x} - x_d$, where x_d explains the desired values of each states. Matrix $\overline{A}_c$ contains all the $a_{i,j}$ elements in (48) which presents the system dynamics. Furthermore, matrix $\overline{B}_c$ contains $b_{i,j}$ elements in (49) which presents the interconnections between the applied torques and corresponding states. $a_{i,j}$ and $b_{i,j}$ can be written as

$$a_{i,j} = \begin{cases} 1 & \text{if } i = 2n-1, \text{ and } j = i+1 \\ 0 & \text{otherwise} \end{cases} \quad (48)$$

and

$$b_{i,j} = \begin{cases} \tau_{tot}\left(\frac{i}{2}, j\right) & \text{if } i = 2n, \\ 0 & \text{otherwise} \end{cases} \tag{49}$$

where $n = 1, \ldots, 6$. Because in any actual system the existence of disturbances, for example, uncertainties in dynamic parameters, is undeniable, an integral controller is employed to eliminate constant disturbances (Åström and Hägglund, 1995). The main control issue extracted from (47) can therefore be reformulated by taking into account integral states (z) of S (i.e., as many as the number of links), explained by

$$\dot{z}(t) = \overline{C}_c \overline{e}(t) \tag{50}$$

where $\overline{C}_c$ includes $\overline{c}_{i,j}$ determined as follows

$$\overline{c}_{i,j} = \begin{cases} 1 & \text{if } i = n, \text{ and } j = 2i - 1 \\ 0 & \text{otherwise} \end{cases} \tag{51}$$

Thus, by integrating the integral states into the state-space formulation, the final dynamic error of the system is proposed as

$$\dot{e} = Ae(t) + B(t)T(t) + d(t) \tag{52}$$

accordingly

$$e = \begin{bmatrix} \overline{e} \\ z \end{bmatrix}, d = \begin{bmatrix} \overline{d}_c \\ 0_{S\times 1} \end{bmatrix} \tag{53}$$

$$A = \begin{bmatrix} \overline{A}_c & 0_{H\times S} \\ \overline{C}_c & 0_{S\times S} \end{bmatrix}, B = \begin{bmatrix} \overline{B}_c \\ 0_{S\times n} \end{bmatrix}, C = \begin{bmatrix} \overline{C}_c & 0_{n\times S} \\ 0_{S\times 2n} & I_{S\times S} \end{bmatrix} \tag{54}$$

5.2. Time-delay control scheme

By assuming a time-delay of η for the system in (52) (η is the summation of all the delays including actuator and sensor), the time-variant form of the system is written as

$$\dot{e}(t) = Ae(t) + BT(t - \eta), y(t) = Ce(t). \tag{55}$$

Accordingly, the solution for the well-known differential equation in (55) is presented in Karafyllis and Krstic (2013)

$$\dot{e}(t) = e^{A_t(t-t_0)}e(t_0) + \int_{t_0}^{t} e^{A(t-v)}BT(v)dv. \tag{56}$$

In the discrete-time domain and considering only one step delay, t can be considered as

$$t_0 = k\ \ \Delta t, t = k\Delta t + \Delta t. \tag{57}$$

Generally, it may happen that the resolution of the time step (Δt) cannot cover the delay of η; then $\eta = \mu\Delta t + \eta_0$ and

$$\begin{aligned} e(k+1) =& e^{A\Delta t}e(k) + \int_0^{\eta_0} e^{A(\Delta t - v)}BdvT(k-1) \\ &+ \int_{\eta_0}^{\Delta t} e^{A(\Delta t - v)}BdvT(k) \end{aligned} \tag{58}$$

where $k\Delta t - \zeta = -v$ and $T(k-1)$ are the delayed outputs of $T(k)$ for one time step. From now on, the μ number of steps delayed output is shown as $T_{k-\mu}$ which is considered as extra states to be a controller as follows

$$e_{1_{dis}} = \begin{bmatrix} e \\ T_{k-1} \end{bmatrix}. \tag{59}$$

Then, the state-space in (58) is formulated as

$$e_{1_{dis}}(k+1) = A_{1_{dis}}e_{1_{dis}}(k) + B_{1_{dis}}T(k) \tag{60}$$

where

$$\begin{aligned} A_{1_{dis}} &= \begin{bmatrix} e^{A\Delta t} & \int_0^{\eta_0} e^{A(\Delta t - v)}Bdv \\ 0_{n\times(N+S)} & 0_{n\times n} \end{bmatrix} \\ B_{1_{dis}} &= \begin{bmatrix} \int_{\eta_0}^{\Delta t} e^{A(\Delta t - v)}Bdv \\ \hline I_{n\times n} \end{bmatrix}, C_{1_{dis}} = \begin{bmatrix} C & 0_{S\times n} \end{bmatrix} \end{aligned} \tag{61}$$

where n is the number of the system inputs, S is the number of integral states, N denotes the number of elements in matrix $\dot{e}$ in (47), and I is the identity matrix. Now, the discrete system with μ steps delay is explained which can be written as

$$\begin{aligned} e_{1_{dis}}(k+1) &= A_{1_{dis}}e_{1_{dis}}(k) + B_{1_{dis}}T_{k-\mu} \\ y(k) &= C_{1_{dis}}e_{1_{dis}}(k). \end{aligned} \tag{62}$$

Considering each delay line of the control signal as a single state of the discrete system and the total number of variables in $e_{1_{dis}}$ as $H = N+S+n$, then the state variable matrix of the discrete system with the new states is

$$e_{dis_{(H+\mu n)\times 1}} = \begin{bmatrix} e_{1_{dis}} \\ e_{dis_{H+1:H+n}} \\ \vdots \\ e_{dis_{H+(\mu-1)n+1:H+\mu n}} \end{bmatrix} = \begin{bmatrix} e_{1_{dis}} \\ T_{k-\mu} \\ \vdots \\ T_{k-1} \end{bmatrix} \tag{63}$$

and, the system with μ-step delay is

$$\begin{aligned} e_{dis}(k+1) &= A_{dis}e_{dis}(k) + B_{dis}T_k \\ y(k) &= C_{dis}e_{dis}(k) \end{aligned} \tag{64}$$

where

$$A_{dis} = \begin{bmatrix} A_{1_{dis}} & B_{1_{dis}} & 0_{H\times(\mu-1)n} \\ 0_{(\mu-1)n\times H} & 0_{(\mu-1)n\times n} & I_{(\mu-1)n\times(\mu-1)n} \\ 0_{n\times H} & 0_{n\times n} & 0_{n\times(\mu-1)n} \end{bmatrix} \quad (65)$$

$$B_{dis} = \begin{bmatrix} 0_{(H+(\mu-1)n)\times n} \\ I_{n\times n} \end{bmatrix}, C_{dis} = [\, C_{1_{dis}} \quad 0_{S\times(H+\mu n)} \,].$$

Now, the following quadratic cost function (Tajdari et al., 2019) can be defined over an infinite time horizon, which is determined for the minimization of all states and control inputs

$$\min J = \sum_{k=0}^{\infty} \left[e_{dis}(k)^T C_{dis}^T Q C_{dis} e_{dis}(k) + T^T(k) R T(k) \right] \quad (66)$$

where

$$Q = \omega_Q I_{(H+\mu n)\times(H+\mu n)}, R = \omega_R I_{n\times n}. \quad (67)$$

The Q and R matrices are weight matrices that tend to minimize the error of all states and the control signals. And, $\omega_Q > 0$ and $\omega_R > 0$ are formulated for weighing matrices.

A linear–quadratic regulator (LQR) is used to solve resultant optimal control problems (66), (67), in which the goal is to stabilize feedback gains via the assumption considering the stability and detectability conditions, fulfilled according to Tajdari et al. (2020a) via the Hautus test (Williams and Lawrence, 2007).

5.3. Controller gains

In order to solve the LQI problem, a linear feedback control law is proposed as follows

$$T(k) = -K e_{dis}(k) \quad (68)$$

where

$$K = \left(R + B_{dis}^T P B_{dis}\right)^{-1} B_{dis}^T P A_{dis}, \quad (69)$$

$$P = C_{dis}^T Q C_{dis} + A_{dis}^T P A_{dis} - A_{dis}^T P B_{dis} \left(R + B_{dis}^T P B_{dis}\right)^{-1}. \quad (70)$$

The result is K in (69) as an optimal gain, and Navvabi and Markazi (2019) investigate the algebraic Riccati equation (70). In addition, in terms of realistic execution, the calculated K is divided into three sections

$$K = [\, K_{\mathrm{P}} \quad K_{\mathrm{I}} \quad K_{\mathrm{U}} \,], \quad (71)$$

leading to the reformulation of the optimum control law as

$$T(k) = -K_{\mathrm{P}} \overline{e}(k) - K_{\mathrm{I}} z(k) - K_{\mathrm{U}} u(k), \quad (72)$$

where $u = [T_{k-1}, T_{k-\mu}, \ldots, T_{k-1}]^T$. For realistic implementations, the final control law (72) is dramatically efficient, as the computational effort regulated by the input benefits K_{P}, K_{I}, and K_{U} presents significantly lower values.

5.4. Anti-windup approach

In functional implementations, due to complexities such as input saturation problems, exact values of the desired states cannot always be obtained. Therefore, the anti-windup system has been incorporated as investigated in Åström and Rundqwist (1989), into the proposed controller. The scheme amends the integral part of the dynamic controller (72) as

$$\begin{aligned} z(k+1) =& (I + \Lambda K_{\mathrm{I}}) z(k) + \left(\overline{C}\Delta t + \Lambda K_{\mathrm{P}}\right) \overline{e}(k) \\ &+ \Lambda K_{\mathrm{U}} u(k) + \Lambda \mathrm{sat}(T(k)) \end{aligned} \quad (73)$$

where $\Lambda \in \mathbb{R}^{S\times n}$ and $(I + \Lambda K_{\mathrm{I}}) \in \mathbb{R}^{S\times S}$. As the torque saturation is virtually included in the actual machine input $T(k)$, the saturation operator is shown below

$$\mathrm{sat}(T_o) = \begin{cases} T_o^{\min}, & \text{if } T_o \le T_o^{\min} \\ T_o^{\max}, & \text{if } T_o \ge T_o^{\max} \\ T_o, & \text{otherwise,} \end{cases} \quad (74)$$

where o determines the index of each controlled input in T, and $T_o^{\min}$ and $T_o^{\max}$ denote the lower and upper limits corresponded to input T_o. Note that the integral states dynamic in (73) reduces to (50), while the $T(k)$ may not reach the saturation limit. Numerical tests further clarify that the T preference of various nominal values has little effect on the execution of the controller and the integral controller's ability to ignore disturbances (Åström and Hägglund, 1995) can be calculated.

5.5. The closed-loop anti-windup system stability analysis

A main restriction to the consistency of the closed-loop structure conveys the matrix Λ, which implies that the stable eigenvalues of $I+\Lambda K_{\mathrm{I}}$ are $\overline{\lambda}$ (Kapoor et al., 1998). For example, this can be accomplished by classic pole placement or a specific algorithm in Kapoor et al. (1998). Notice that when inputs are not saturated, the stability of the system is shown by the Hautus test in Williams and Lawrence (2007), whereas Λ must be constructed accordingly if inputs are saturated, since it may affect the stability of (73). For (52) stability analysis, it is reworded as

$$e_{dis}(k+1) = \overline{\overline{A}} e_{dis}(k) + (B + R_{\mathrm{aw}}\Lambda)\mathrm{sat}(T(k)), \quad (75)$$

where

$$R_{\text{aw}} = \begin{bmatrix} 0_{N\times S} \\ I_{S\times S} \\ 0_{\mu n\times S} \end{bmatrix}, \overline{\overline{A}} = \begin{bmatrix} \overline{A}(1:N,:) \\ \left[\overline{C}\Delta t + \Lambda K_P, I + \Lambda K_I, \Lambda K_U\right] \\ \overline{A}(H+1:end,:) \end{bmatrix} \tag{76}$$

Referring to da Silva and Tarbouriech (2006), if a symmetric positive definite matrix is found as $W_{\text{aw}} \in \mathbb{R}^{(H+S)\times(H+S)}$, a diagonal positive definite matrix is found as $S_{\text{aw}} \in \mathbb{R}^{F\times F}$, and a matrix is found as $Z_{\text{aw}} \in \mathbb{R}^{S\times F}$, subject to

$$\Xi = \begin{bmatrix} W_{\text{aw}} & -W_{\text{aw}}K' & -W_{\text{aw}}A' \\ -KW_{\text{aw}} & 2S_{\text{aw}} & SB' + Z'_{\text{aw}}R'_{\text{aw}} \\ -AW_{\text{aw}} & BS_{\text{aw}} + R_{\text{aw}}Z_{\text{aw}} & W_{\text{aw}} \end{bmatrix} > 0 \tag{77}$$

then, for $Z_{\text{aw}} = \Lambda S_{\text{aw}}$, the system in (75) is globally asymptotically stable. In this formulation, the matrix W_{aw} can be specified as follows

$$W_{\text{aw}} = \zeta I_{(H+S)\times(H+S)}, \tag{78}$$

where a single parameter is a ζ that should be determined correctly. This analysis reveals that the global asymptotic stability of the closed-loop system can be dealt with when optimizing controller parameters by testing the condition of (77) for a reasonable domain of $\overline{\lambda}$ and ζ. This shows the global robustness of the closed-loop system, as defined in Khalil and Grizzle (2002), in the presence of disruptions and uncertainties.

5.6. Sensitivity analysis

To evaluate the suggested technique, the dynamic compensators (72) and (73) are added to the nonlinear ADAMS model, while $\overline{\lambda}$ is known as 0.5 for all the 6 stable poles of $I+\Lambda K_{\text{I}}$ in (73). Next, a series of tests are conducted to set the parameters of the controller. In the 10 (s) time-domain experiments, the time step is considered to be Δt = 0.1 (s) (corresponding to the frequency implemented in the Experiment Setup section). As follows, the defined variables $(\overline{X}_d)$ are modified

$$\begin{aligned} \overline{X}_d(t) &= [\varphi_d(t), \theta_d(t), \psi_d(t), x_d(t), y_d(t), z_d(t)]^T \\ &= \left[\frac{\pi}{12}, \frac{\pi}{12}, \frac{\pi}{12}, 0.04, 0.04, .08\right]^T Sin(t) \\ &+ [0, 0, 0, 0, 0, .38]^T \end{aligned} \tag{79}$$

As discussed in the Adaptive Time-Delay Estimator Design section, a reference model should be built with stable dynamics, where one of the states is the integral of the other state. Thus, a two-state system is used with a globally stable dynamic around r_e, as follows

$$\dot{X}_r = A_r X_r + B_r r_e \tag{80}$$

$$A_r = \begin{bmatrix} 0 & 1 \\ -10 & -2 \end{bmatrix}, B_r = \begin{bmatrix} 0 \\ 10 \end{bmatrix}, \tag{81}$$

where $X_M = X_{r_{1,1}}$. Studying the sensitivity of the controller (Tajdari et al., 2022c) to the parameters w_Q, w_R, $\overline{\lambda}$, v_1, and v_2 selection, employing as evaluation metric is utilized as the average percentage of final error E_p composed of E_{p_i} corresponded to each variables of matrix $\overline{X}$ in (1) as

$$E_{p_i} = \frac{\overline{X}_i^{t_{end}} - \overline{X}_{d_i}^{t_{end}}}{A_{m_i}} \times 100. \tag{82}$$

In (82), i = 1, ..., $H/2$, t_{end} = 10 (s), and A_{m_i} indicates the peak-to-peak amplitude of the desire values $(\overline{X}_{d_i})$ of relative variable $(\overline{X}_i)$ (for the cases that desire is constant, A_{m_i} is considered as 1). Thus, the average percentage of final error $(\overline{E}_p)$ is formulated as

$$\overline{E}_p = \frac{2}{H}\sum_{i=1}^{\frac{H}{2}} E_{p_i}. \tag{83}$$

It can be inferred from Figure 2 (top-left) related to the no-time-delay experiments, which demonstrates how the $\overline{E}_p$ obtained varies by pairing the weights (w_Q and w_R) used in cost functions (66) and (67). Regarding Figure 2(top-right), where μ = 8, the values of $\overline{E}_p$ over the variations of the parameters v_1 and v_2 employed in the adaptive estimator in (44) are depicted. The presented analysis in this figure enables the controller to acquire a low value of $\overline{E}_p$ (blue areas) for a broad variety of parameters. Accordingly, w_Q = 1, w_R = 4, v_1 = 2, and v_2 = 2 are selected from the blue areas as they have the least sensitivity. This illustrates the benefit of the controller in specifying the parameters, explains less work to adjust the control parameters in order to achieve acceptable results. Since appropriate results are obtained from computational experiments (with an acceptable $\overline{E}_p$), there are, however, some cases (e.g., the saturation of multiple inputs) that may not occur in software simulations. These instances can result in unstable conditions for the system.

In line with the Closed-Loop Anti-Windup System Stability Analysis section, the stability of the closed-loop system is investigated. In other words, it evaluates if the Ξ matrix in (77) is a positive definite matrix for a large variety of $\overline{\lambda}$ and ζ. In order to be succinct, the results for $\overline{\lambda} \equiv \overline{\lambda}_1 = \ldots = \overline{\lambda}_6$ are clarified in Figure 2(bottom-left), which demonstrates that there are no unstable values for the $0 \leq \overline{\lambda} \leq 1$ region. This inferred that Ξ is positive definite. As a consequence, this indicates that the apportion of $\overline{\lambda}_1, \ldots$ and $\overline{\lambda}_6$ within the $(0, 1)$ set provides accurate results in terms of $\overline{E}_p$ (Figure 2(bottom-left)) and maintains the asymptotic consistency of the closed-loop system. Therefore, $\overline{\lambda}$ is

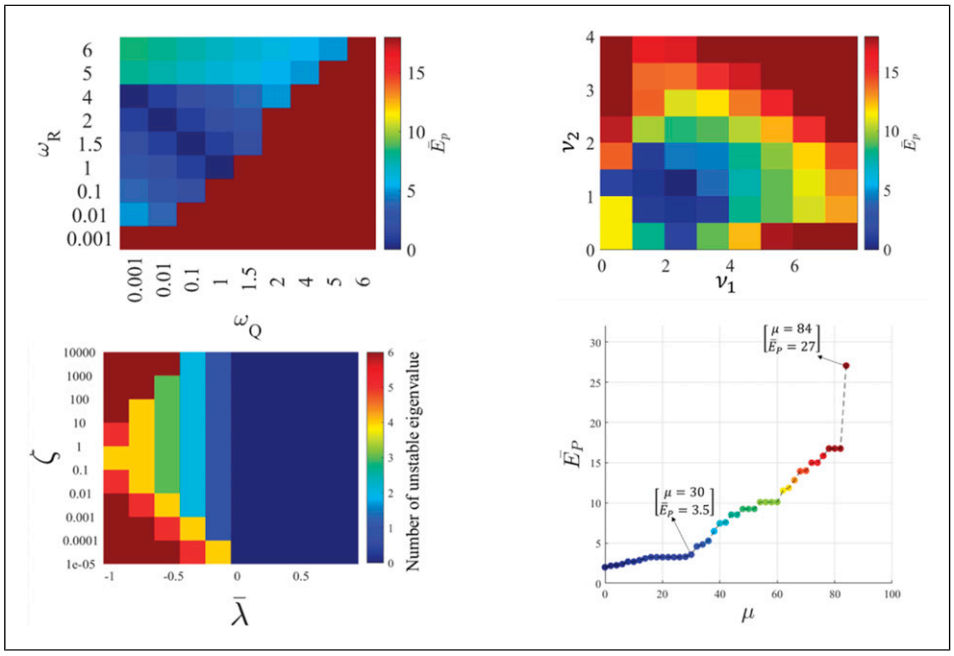

Figure 2. Numerical analysis: Sensitivity analysis based on $\bar{E}_p$ for a domain of w_Q and w_R, where $\bar{\lambda} = 0.5$, $\nu_1 = 2$, and $\nu_2 = 2$ (top-left). Sensitivity analysis based on $\bar{E}_p$ for a domain of ν_1 and ν_2, where $\bar{\lambda} = 0.5$, $w_Q = 1$, and $w_R = 4$ (top-right). Number of negative eigenvalues in Ξ, where $w_Q = 1$, $w_R = 4$, $\nu_1 = 2$, and $\nu_2 = 2$ for a domain of $\bar{\lambda}$ and ζ (bottom-left). Sensitivity analysis based on $\bar{E}_p$ for a domain of μ, where $\bar{E}_p$ while $w_Q = 1$, $w_R = 4$, $\nu_1 = 2$, $\nu_2 = 2$, and $\bar{\lambda} = 0.5$ (bottom-right).

picked as $\bar{\lambda} = 0.5$. According to Figure 2(bottom-left), global system stability has the lowest sensitivity of $\bar{\lambda}$ at this point as the point is located in the middle of the dark blue area.

In addition, the sensitivity of the delayed steps to the performance of the robot reveals the allowed domain of delay which should be considered in the design of the robot during the motor selection process. To this end, a set of experiments is performed to investigate the effects of μ in domain of 0–100 in terms of $\bar{E}_p$ while $w_Q = 1$, $w_R = 4$, $\nu_1 = 2$, $\nu_2 = 2$, and $\bar{\lambda} = 0.5$. The results of the experiments are reported in Figure 2(bottom-right) which shows that the speed of error is increasing at $\mu = 30$, and after $\mu = 84$, there is no value for $\bar{E}_p$ as robot's dynamic states passed the allowed work-space. Thus, the acceptable performance of the controller is in the domain of $0 \leq \mu \leq 30$ which has the least error highlighted with dark blue color in Figure 2(bottom-right).

5.7. ANN estimator design for w_Q and w_R

Since the parameters of dynamic equations in (46) are time-variants, $B_{dis}(k)$ in (64) is accordingly time-variant regarding (49). Thus, in answer to the particular direction, it is theoretically assumed that the mechanism has different behavior in different directions. Accordingly, the use of intelligent methods means nonlinearity of the mechanism and the optimization process, and complexity of the problem. Since the cost function of the optimal problem in (66) is based on w_Q and w_R, estimating the true values of w_Q and w_R in each step is a solution to the nonlinearities, where w_Q determines the degree of the penalization of the error of the states, and w_R optimizes the torques built. An advanced artificial neural network (ANN)–based input–output estimator is therefore designed to estimate w_Q and w_R online, where state error functions and torque functions are selected parameters as the estimator's inputs. The functions introduced in Tajdari and Toulkani (2021) imply that for any arbitrary variable of ϵ, the density function is

$$\rho_\epsilon(k) = \Omega_\epsilon(\epsilon(k)) = (w_{in} + 1)\frac{\epsilon(k)}{\sum_{i=k-w_{in}}^{k}\epsilon(i)} \tag{84}$$

where ρ_ϵ is the density of the variable. Actually, (84) is sensitive when $\epsilon(k)$ is sufficiently greater than average of the variable with window size w_{in}+1. The criterion explains a smooth and logical stimulation to changes of the variable (Tajdari and Toulkani, 2021). Consequently, the inputs of the intelligent estimator are $\rho_{\bar{e}_{1\times 6}}$ and $\rho_{T_{1\times 6}}$, and the outputs are $w_{Q_{1\times 1}}$ and $w_{R_{1\times 1}}$ as shown in Figure 3(a). To design an ANN-based estimator, a set of data including the inputs–output is essential. Therefore, the controller of (72) with integral states of (73) is used as a master for the estimator. To collect data, the output of the controller is used, while $w_{in} = 30$, $T_o^{\max} = 1.5$ N.m, and $T_o^{\min} = -1.5$ N.m, and $\mu = 0$, 5, 10, 20, and 30 steps. And for the controller parameters, the blue area was selected in Figure 2(top-left), where $0.1 \leq w_R \leq 4$ and $w_R > w_Q$. To consider the effects of the frequency

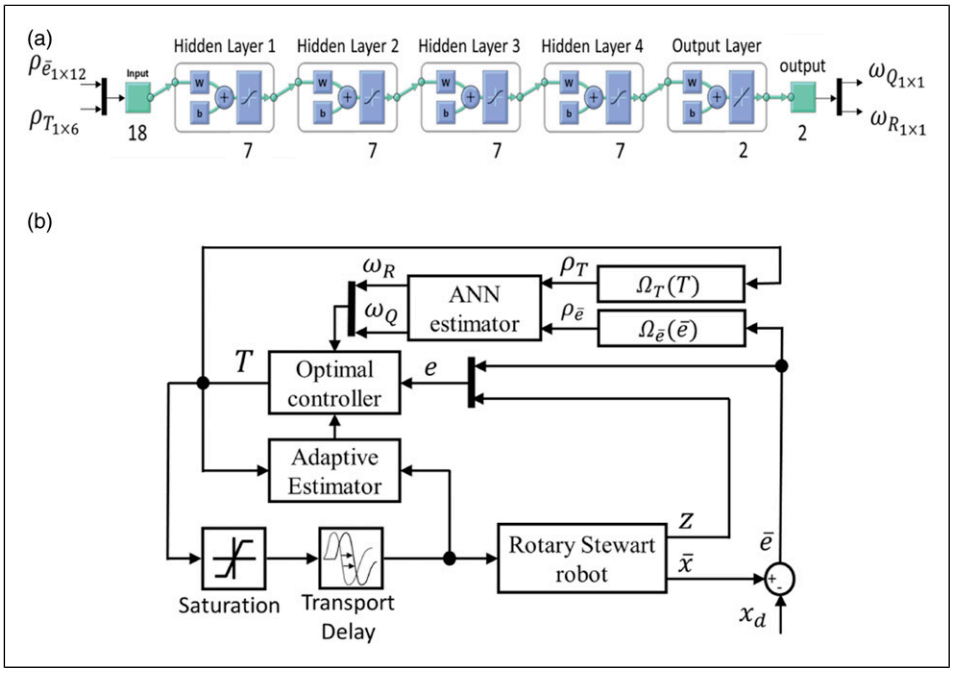

Figure 3. The schematic structure: (a) designed ANN estimator structure and (b) closed-loop control diagram.

of the desired values, the mentioned experiments were repeated with the frequencies of 0.5, 2, 4, and 6 Hz; thus, the final data-set consists of 375 experiments, and during all the experiments, the sample time is 0.1 s, and spent-time is 10 s. This concludes with the input–output data-set with 37,500 samples. The ANN estimator uses the back-propagation algorithm provided in Kosko and Burgess (1998) to train unknown estimator parameters. Therefore, randomly selected 70% of the data-set is considered for training (Tajdari et al., 2017b), and the remaining 30% is used to validate the obtained model. The structure of the ANN estimator is designed through numerical solutions. Regarding Table 2(a), the error of $\overline{E}_p$ is extracted for a different number of hidden layers and a different number of nodes through running the simulated system with the same conditions used to collect the training data of the ANN estimator. The table shows the network consists of 4 hidden layers and 7 nodes and has the minimum error which is used as the final structure of the estimator shown in Figure 3(a). Figure 3(b) shows the closed-loop optimal feedback control diagram of the proposed system where the estimator updates the controller gains of w_Q and w_R in each time step regarding the density functions.

To assess the stability of the final structure of the ANN estimator, the input section of the training data-set is used as the input of the estimator, and the output of the estimator is compared with the output section of the training data-set. For the comparison, mean absolute percentage error (MAPE), Standard deviation error (SDE), and correlation coefficient (R^2) are used which are explained in Ghaffari et al. (2018). Accordingly, the estimator has an average value of 0.081 and 0.064 in terms of MAPE and SDE, respectively, explaining a small error with the desired output data. In addition, the R^2 average value of 0.98 defines a high correlation between the output of the estimator and the desired output data, which shows a stable performance of the estimator.

5.8. Robustness level

In order to evaluate the degree of robustness of the controller to the unknown disturbances and uncertainty, the closed-loop control system is experimentally assessed with the parameters discussed in the Sensitivity Analysis section through the ADAMS model in presence of white noise with a variety of amplitudes both on the input torque of the system and the mass value of the end-effector. Accordingly, the implemented torques ($T(k)$) in (75) and mass (m) in (18) are replaced with $\tilde{T}(k)$ composed of $\tilde{T}_i(k)$ (where i shows corresponding index of each controlled input inside vector $\tilde{T}$) and $\tilde{m}(k)$ as the following

$$\begin{aligned} \tilde{T}_i(k) &= T_i(k) + \eta_T T_i^{\max} \xi_i^T(k) \\ \tilde{m}(k) &= m + \eta_m m \xi^m(k) \end{aligned} \tag{85}$$

where ξ_i^T and ξ^m are the random number generators (RNGs) that randomly suggest a number in the domain [0, 1] in each time step. By implementing (85) in (18), and (75), the robustness of the proposed controller is investigated through a set of numerical experiments for a domain of η_T and η_m in range [0, 0.5]. The results of the experiments are reported in Figure 4, which implies that the controller has

Table 2. Structural information.

(a) $\overline{E}_p$ value per different structure of the ANN estimator

	Number of nodes									
Number of hidden layer	1	2	3	4	5	6	7	8	9	10
1	28.6	24.4	20.9	17.9	15.5	13.8	12.9	10.1	11.9	12.1
2	23.7	20.1	17.1	14.5	12.4	11.1	10.6	8.1	10.4	11.1
3	19.6	16.5	14.1	11.8	10.1	6.7	6.5	2.7	4.1	4.7
4	18.1	15.4	13.1	11.1	9.5	6.1	2.1	3.1	3.4	3.9
5	17.1	14.8	12.9	11.1	10.1	3.1	2.7	3.1	13.4	3.4

(b) Motor specifications

Item	Description
Resolution	4096 (pulse/rev)
Dimensions (W × H × D)	40.2 × 61.1 × 41 (mm)
Stall torque	5.5 (Nm) (at 11.1 (V), 3.9 (A))
Physical connection	RS485/TTL Multidrop Bus

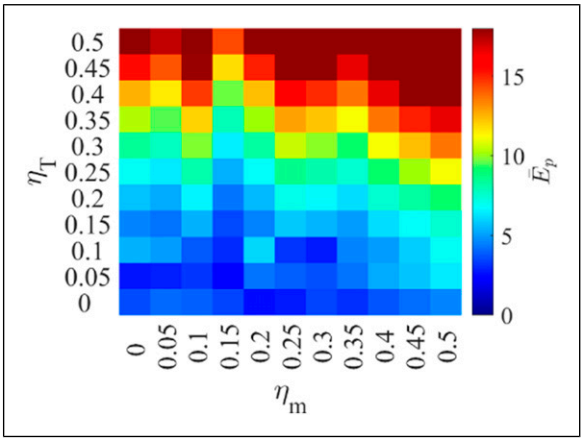

Figure 4. Reported $\bar{E}_p$ for a domain of η_m and η_T.

Figure 5. Fabricated rotary parallel robot.

acceptable performances in terms of $\overline{E}_p$ for huge noise on m (i.e., the domain of $\eta_m \leq 0.45$, which is blue area), as it was expected regarding the features of the integral controller able to reject the unknown disturbances. However, the controller fails when the disturbances on the torques are comparatively high (i.e., the domain of $\eta_T > 0.3$, which is the red area). This happens because there are no possible control actions as most of the torques are saturated, and practically, the controller has not any role in the behavior of the system.

6. Experiment setup

The robot in Figure 1 is generated to test the controller in an actual nonlinear system of natural disturbances. As shown in Figure 5, 6 servo motors of mx-64, with the specifications explained in Table 2(b) of Robotis (2019), are used as torque manipulators and are operated directly by MATLAB software through USB2Dynamixel (Robotis, 2019). In addition, a 9-DOF absolute IMU fusion breakout-BNO055 is used to calculate the end-effector position and angles $(\overline{X})$, and sensor data will be filtered and imported into the MATLAB via Arduino Mega 2560. The BNO055 sensor, located in the center of the end-effector, spits out Euler

angles and vectors as mentioned in Adafruit (2019). The final product frequency for the transmission and receiving of data is roughly 10 Hz. In addition, the motor saturation limit is set to 1.5 N.m due to safety and motor damage prevention.

7. Results

The simulation and experiment results are generated by implementing the proposed controller (72), with integral states in (73), where $w_{in} = 30$, $\mu = 8$, $\Delta t = 0.1$ s, $T_o^{\max} = 1.5$ N.m, $T_o^{\min} = -1.5$ N.m, $v_1 = 2$, and $v_2 = 2$ on the ADAMS model in the Nonlinear Model section and the manufactured robot in the Experiment Setup section, while the desired variables $(\overline{X}_d)$ are considered as following

$$\begin{aligned}\overline{X}_d(t) &= [\varphi_d(t), \theta_d(t), \psi_d(t), x_d(t), y_d(t), z_d(t)]^T \\ &= \left[\frac{\pi}{12}, \frac{\pi}{12}, \frac{\pi}{12}, 0.02, 0.02, .08\right]^T Sin(t) \\ &+ [0, 0, 0, 0, 0, .38]^T\end{aligned} \tag{86}$$

where t is the time. $m = 4$ kg and $m = 5$ kg are considered for the simulation tests and experiment tests, respectively. Six control methodologies are compared in total as

- Controller i: LQR controller.
- Controller ii: LQI controller without anti-windup scheme.
- Controller iii: Time-delay LQI controller with anti-windup scheme.
- Controller iv: Time-delay LQR controller with ANN estimator.
- Controller v: Time-delay LQI controller with ANN estimator and with anti-windup scheme.
- Controller vi: Time-delay LQI controller with ANN estimator and without anti-windup scheme.

7.1. Simulation results

Figure 6 (left) shows the main states for the case $m = 4$ kg, and although controllers i and ii are theoretically stable without any actuator delay as discussed in Tajdari et al. (2020a), they cannot control the robot in presence of the time-delay (cyan and purple line) due to the singularity of the robots dynamic (resulted from the instability of pair $(\overline{A}_c, \overline{B}_c)$ in (47)). However, other controllers iii, iv, and v introduced in the Controller Gains section present a stable performance with finite errors. Controller v performs to achieve perfect tracking

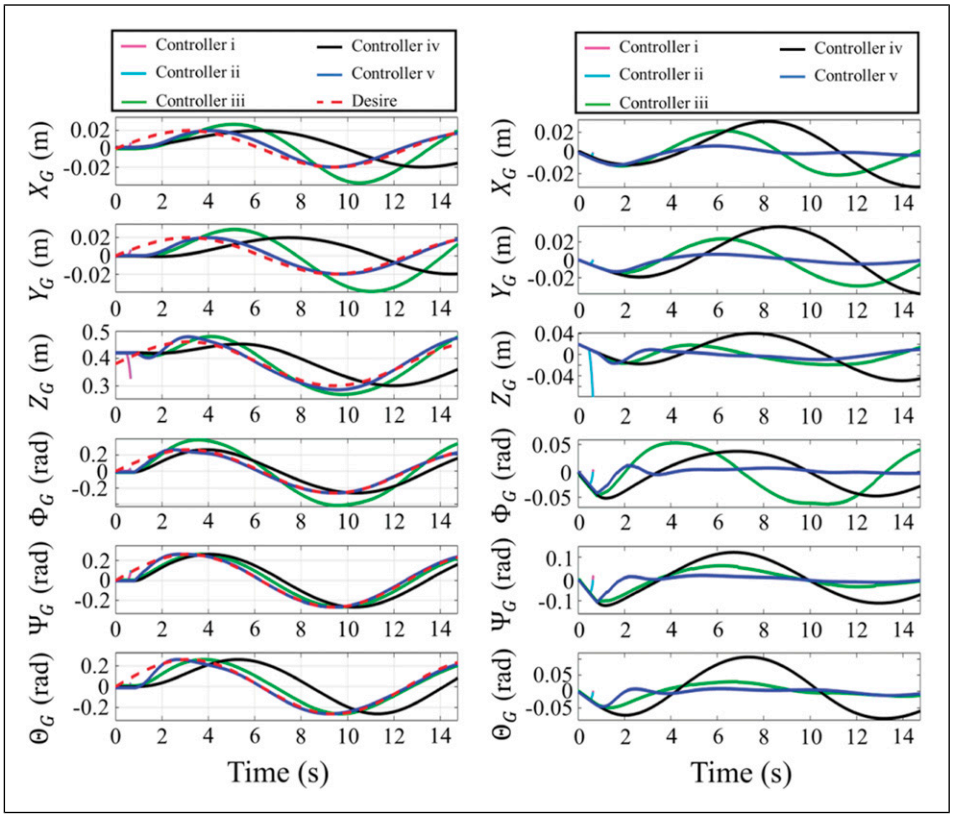

Figure 6. Controlled case performance through the ADAMS model where $m = 4$ kg. Main states $(\overline{X})$ (left). Error of main states $(\overline{X} - \overline{X}_d)$ (right).

(looking at the blue line in Figure 6(left)) and rejects the errors by the time as shown in Figure 6(right). The error reduction has been concluded by the zero-error feature of the integral states and with the well-specified controller time-variant parameters of w_Q and w_R reported in Figure 7 (right). However, the controller iv produces considerable errors, especially in the critical points of the desired path. The performances of the controller iv (black line) regarding the x, y, and z in Figure 6(right), show the deviation, although the controller tries to generate a resemble periodic movement similar to the desire values, and the estimated parameters presented in Figure 7(left). In addition, the performance of the adaptive time-delay estimator is depicted in Figure 8 (left), (right), and (bottom) for controllers iii, iv, and v, respectively. Here, only a single graph is reported for each experiment as the estimated values were the same for each of the motors regarding each of the controllers because equal constant delay is considered for the motors ($\mu = 8$). To compare the results numerically concerning the monitoring error, a criterion with the accumulated absolute percentage error E_{ac} is added as

$$E_{ac} = \frac{2}{H}\sum_{i=1}^{\frac{H}{2}}\int_0^t \left(\frac{\left|\overline{X}_i(t) - \overline{X}_{d_i}(t)\right|}{A_{m_i}} \times 100\right) dt \qquad (87)$$

where E_{ac} is the sum of all absolute amounts, from the beginning to the end of the simulation, where $i = 1, \ldots, H/2$, $t_{end} = 10$ s, and A_{m_i} represent the peak-to-peak magnitude of the desired values $(\overline{X}_{d_i})$ of the relative vector $(\overline{X}_i)$ (where the desire is constant, A_{m_i} is presumed to be 1). The output of the controllers is then defined separately based on the parameters in Table 3(a). As for the table, all controllers without the time-delay scheme (controllers i and ii) failed as expected, at around $t = 0.7$ s as shown in Figure 6(left and

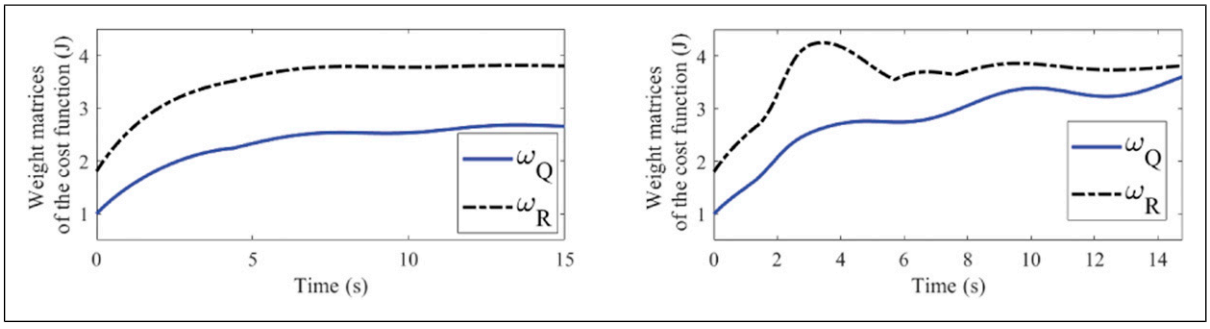

Figure 7. Online estimated w_Q and w_R, where m = 4 kg. Controller iv (left). Controller v (right).

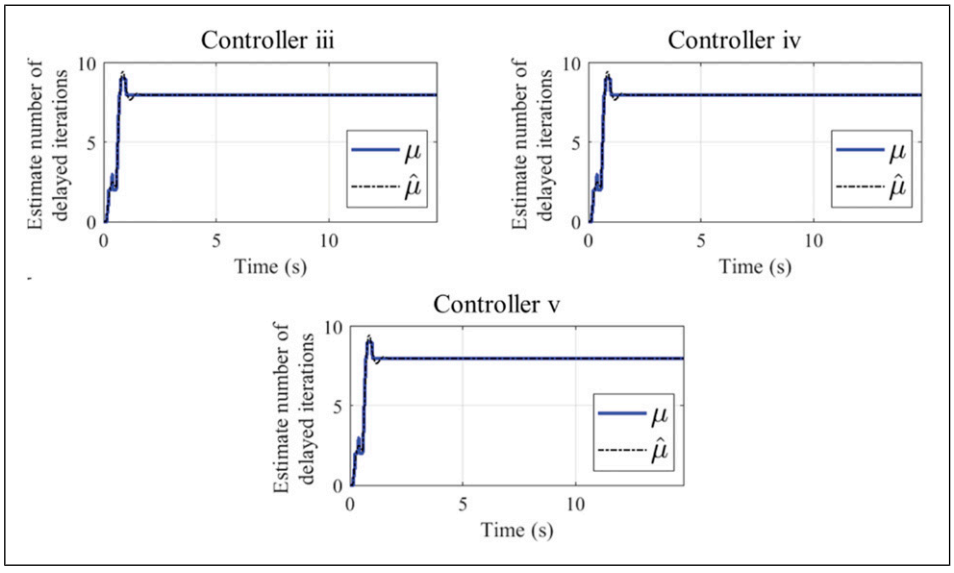

Figure 8. Online estimated of μ in the simulation case, where m = 4 kg.

Table 3. Accumulative absolute percentage error (E_{ac}) report through the ADAMS model for the simulation case and through the fabricated robot for the experimental case.

(a) Where m = 4 kg

Controller	i	ii	Iii	iv	v
E_{ac}	NaN	NaN	713.81	1648.03	192.56

(b) Where m = 5 kg

Case	Controller	E_{ac}
Simulation	v	260.01
	vi	NaN
Experiment	v	293.45

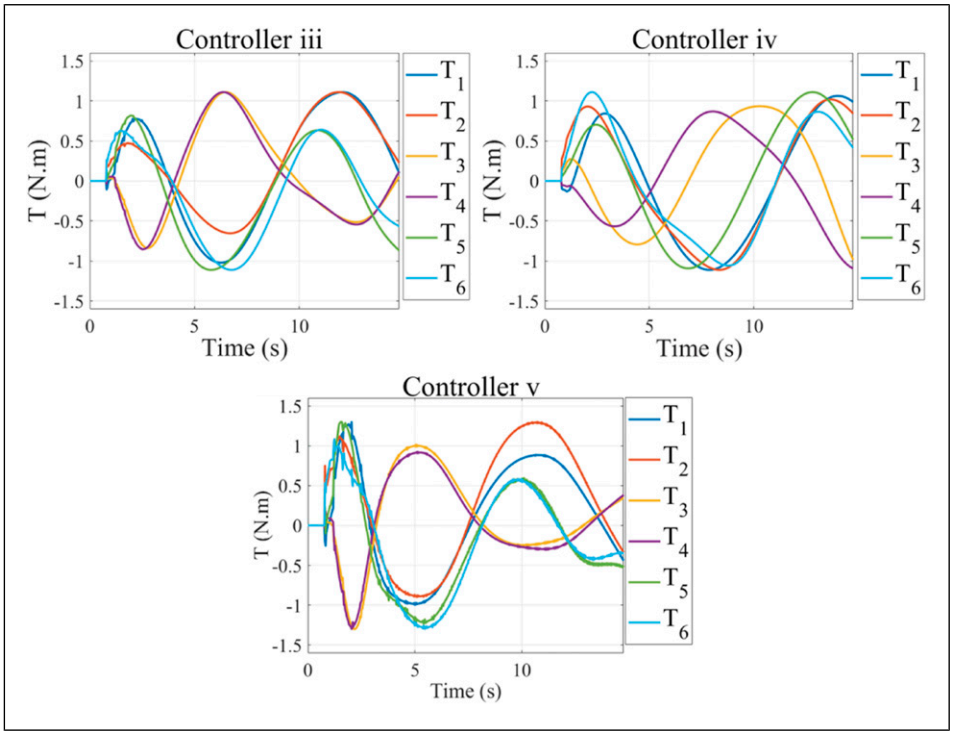

Figure 9. Motor torques in the simulation case, where m = 4 kg.

right). Although time-delay controllers iii, iv, and v kept the system in the allowed work-space according to Table 3(a), controller v had a significant advantage for 73% and 88% over controllers iii and iv, respectively. This reflects the advantages of integrating the integral states and the ANN estimator's ability to reject disturbances and uncertainties.

In comparison, Figure 9 displays the torques that have been applied to the device for the three time-delay controllers iii, iv, and v. Comparing the torques in Figure 9(left, and bottom) with Figure 9(right), the control effort generated by controllers iii and v are reduced by the time as the errors are decreasing. Also, the controllers' torques have more trembling (from t = 0(s) till t = 5(s)) compared to controller iv that resulted from more sensitivity of the integral states to the tracking error due to (50), while the amplitude of the control signals generated by controller iv is increasing due to considerable tracking error. Regarding the figure, no saturation is observed due to the end-effector light mass selection as m = 4 kg. However, in practical applications, saturation

may accrue. Thus, two more simulation experiments were performed via controllers v and vi where $m = 5$ kg to study the impact of the anti-windup scheme, as shown in Figure 10. Accordingly, controller vi (purple line) shows unstable performance and made the system to be stopped around $t = 4$(s) as the states passed the allowed workspace domain. In contrary, the controller v reveals a stable performance by converging the controller's and estimator's parameters in Figure 11(left) and 8 and reducing tracking error by the time. Regarding the controller v, the torques are saturated for a while depicted in Figure 13(right) specifically from t=0(s) till t=5(s).

7.2. Experiment results

The controller v is applied on the robot introduced in the Experiment Setup section to verify and investigate the efficiency of the proposed controller in the case of actual disturbances and uncertainties. The same desire values in (86) are used to compare the simulation

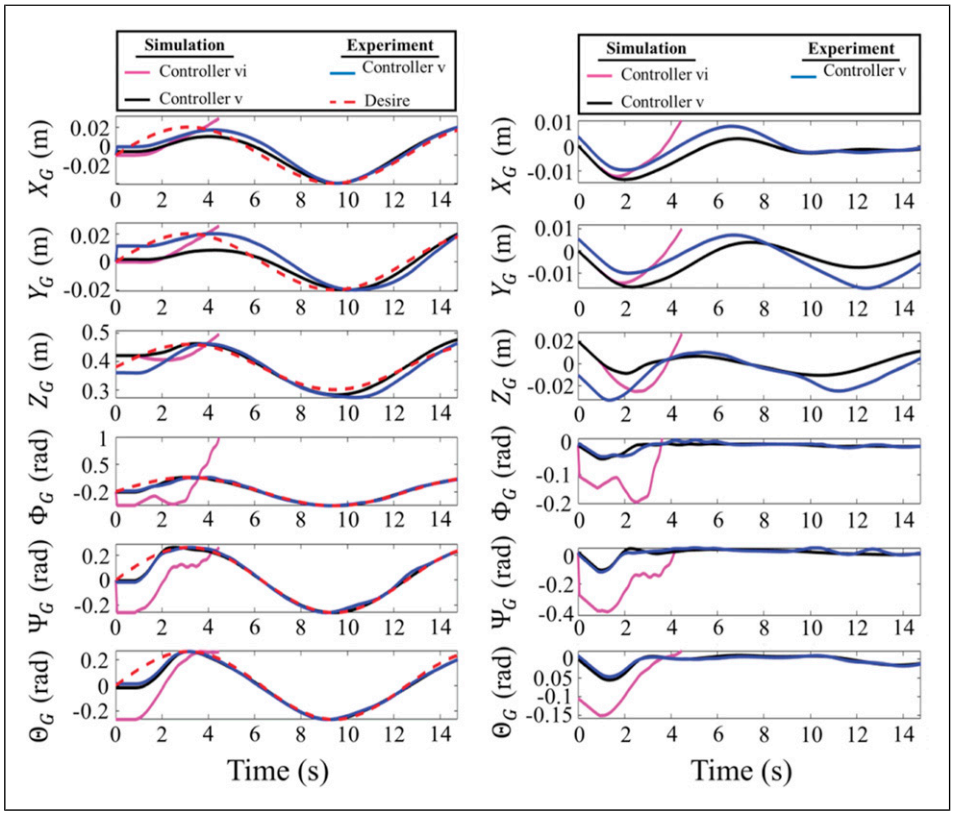

Figure 10. Controlled case performance where $m = 5$ kg. Main states $(\overline{X})$ (left). Error of main states $(\overline{X} - \overline{X}_d)(\overline{X} - \overline{X}_d)$ (right).

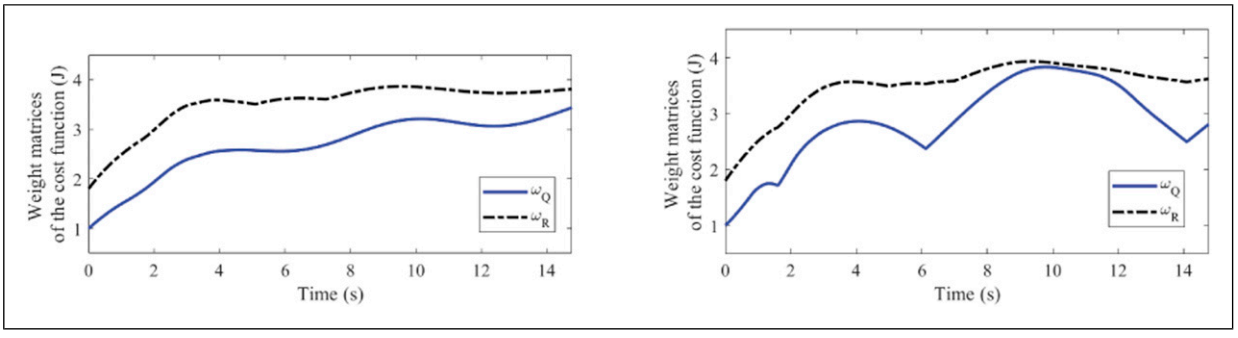

Figure 11. Online estimated w_Q and w_R with controller v, where $m = 5$ kg. Simulation case (left). Experiment case (right).

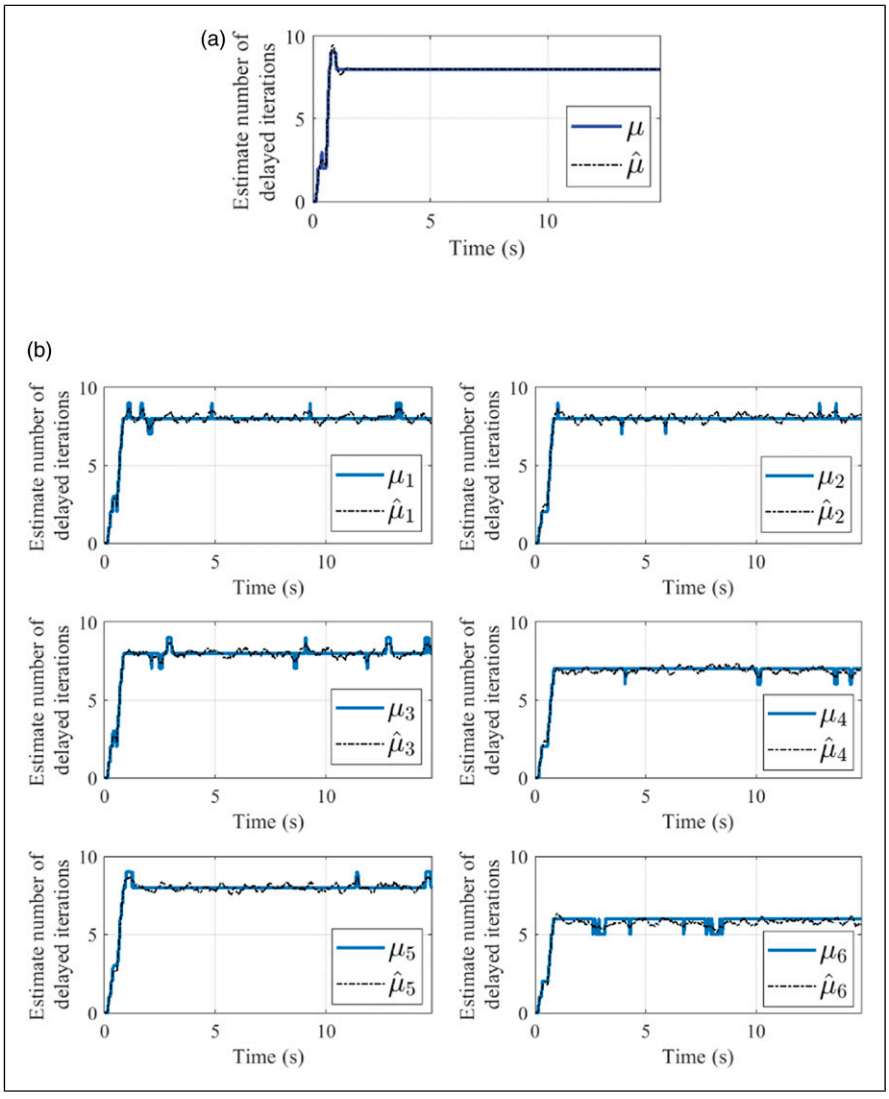

Figure 12. Online estimated of μ using controller v, where m = 5 kg: (a) simulation case and (b) experiment case per each motor.

output. All other control parameters and initial conditions are assumed to be the same as the Simulation Results section, and m = 5 kg. In Figure 10(left), the controller performances in the main states are described. And comparing the effects of the controller v in simulation and experimental tests, Figure 10(right) reveals that the proposed controller is stable enough to sustain zero-error convergence in the face of natural uncertainties and disruptions. The output of the controllers is then defined separately based on the parameters in Table 3(b). According to the table, only the controller with the anti-windup scheme could keep the states in the allowed work-space and thus the controller vi failed due to the saturation accrued as in Figure 13(left). Regarding the table, the other controller v, for both cases of the simulation and experiments shows acceptable performance. Looking at the approximate w_Q and w_R trajectories in Figure 11, controller v has appropriate actions in both situations, and the output is more fluctuating in the experimental case as the ANN estimator attempts to resolve more uncertainties, that is, resolution of sensors, unpredictable internal time-delays, and natural disruptions. In addition, the estimated time-delay depicted in Figure 12(b) is different from a motor to another motor contrary to the simulation results in Figure 12(a), although the same time-delay value is manually manipulated for the servo motors. This may happen because of the sensor lag and other unknown delays of the motor gearbox, etc. Accordingly, although the torques in Figure 13 (bottom) are saturated for several time intervals, especially for T_1, the controller shows stable and zero-error

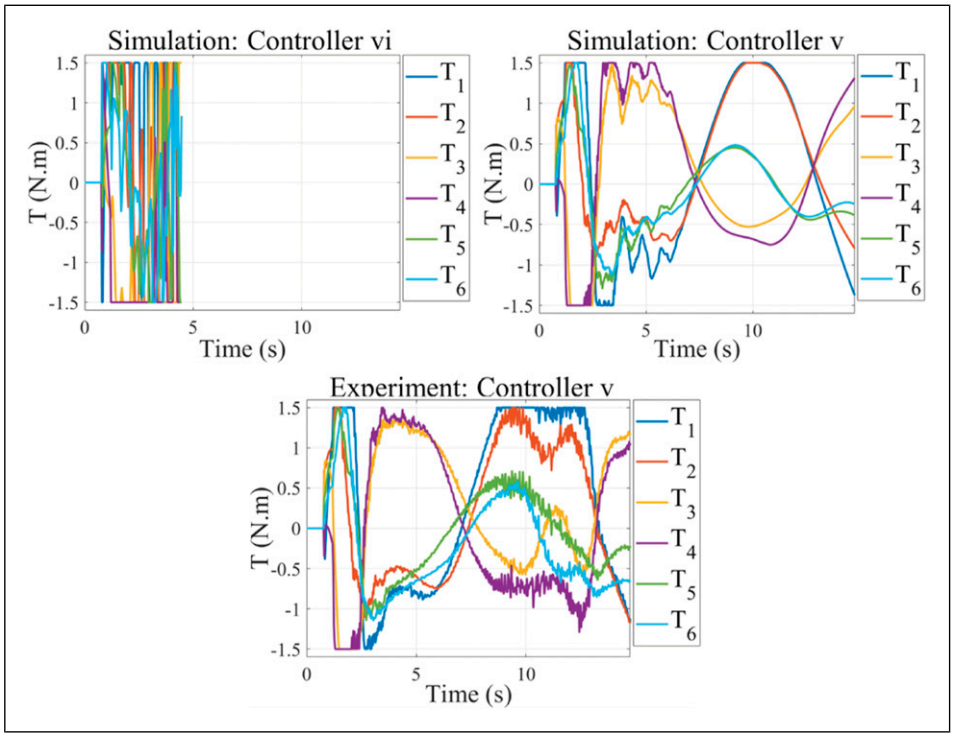

Figure 13. Motor torques, where m = 5 kg.

convergence thanks to the well-designed estimator and the anti-windup scheme.

8. Conclusion

This paper investigates a novel robust control methodology integrated with an innovative adaptive time-delay estimator for a Stewart parallel robot integrated with the delayed rotary actuator. To achieve the desired value of the end-effector states, the implemented robot dynamic in ADAMS software is controlled online through the intelligent time-delay tuning of the LQI controller's parameter. The robustness, as well as the adaptive estimator scheme, that is, the ANN estimator, elaborates on easy practical implementation, without the need for lengthy and costly measurements of the dynamic parameters. Furthermore, the simulation outputs depicted that the proper time-delay LQI controller with an intelligent estimator outperformed the other compared methods to control the dynamics of the device and eliminate the error of controlling in presence of the disturbing dynamic forces and the huge delay of the actuators in the ADAMS model. According to the validation of the controller through practical implementation of the controller on a fabricated robot, the perfect tracking was achieved and the TDE was successful. Further improvements contain designing an adaptive estimator with self-tuning the growth ratio of the adaptation rule emphasizing a more automated framework. In addition, a more complex robot platform will be discussed by mounting a second Stewart robot on the end-effector of the discussed robot in this paper which may challenge the proposed controller.

Declaration of conflicting interests

The author(s) declared no potential conflicts of interest with respect to the research, authorship, and/or publication of this article.

Funding

The author(s) disclosed receipt of the following financial support for the research, authorship, and/or publication of this article: This work is partly supported by Dutch NWO Next UPPS—Integrated design methodology for Ultra Personalised Products and Services project under Grant 15470.

ORCID iD

Farzam Tajdari https://orcid.org/0000-0001-7378-0368

References

Adafruit (2019) Adafruit 9-DOF absolute orientation IMU fusion breakout - BNO055. URL: https://www.adafruit.com/product/2472l

Åström KJ and Hägglund T (1995) *PID Controllers: Theory, Design, and Tuning*, Vol. 2. NC: Instrument society of America Research Triangle Park.

Åström KJ and Rundqwist L (1989) Integrator windup and how to avoid it. In: 1989 American Control Conference, Pittsburgh, PA, USA, 21-23 June 1989.

Baek J, Cho S and Han S (2017) Practical time-delay control with adaptive gains for trajectory tracking of robot manipulators. *IEEE Transactions on Industrial Electronics* 65(7): 5682–5692.

Baek S, Lee H and Han S (2021) Communication-efficient event-triggered time-delay control and its application to robot manipulators. *IEEE Transactions on Industrial Electronics* 69: 9288–9297.

da Silva JG, Jr and Tarbouriech S (2006) Anti-windup design with guaranteed regions of stability for discrete-time linear systems. *Systems & Control Letters* 55(3): 184–192.

Fu D, Zhao X and Yuan H (2022) Nonsingular terminal sliding mode control based on adaptive time delay estimation for permanent magnet linear synchronous motor. *International Journal of Control, Automation and Systems* 20(1): 24–34.

Ghaffari A, Khodayari A, Kamali A, et al. (2018) New fuzzy solution for determining anticipation and evaluation behavior during car-following maneuvers. *Proceedings of the Institution of Mechanical Engineers - Part D: Journal of Automobile Engineering* 232(7): 936–945.

Hu M, Li C, Bian Y, et al. (2022) Fuel economy-oriented vehicle platoon control using economic model predictive control. *IEEE Transactions on Intelligent Transportation Systems* 23: 20836–20849.

Huang CI and Fu LC (2004) Adaptive backstepping tracking control of the stewart platform. In: 2004 43rd IEEE Conference on Decision and Control (CDC)(IEEE Cat. No. 04CH37601), Nassau, Bahamas, 14–17 December 2004, vol. 5: IEEE, pp. 5228–5233.

Huang Q, Lan J and Li X (2018) Robotic arm based automatic ultrasound scanning for three-dimensional imaging. *IEEE Transactions on Industrial Informatics* 15(2): 1173–1182.

Jin M, Kang SH, Chang PH, et al. (2017) Robust control of robot manipulators using inclusive and enhanced time delay control. *IEEE* 22(5): 2141–2152.

Jin M, Lee J and Tsagarakis NG (2016) Model-free robust adaptive control of humanoid robots with flexible joints. *IEEE Transactions on Industrial Electronics* 64(2): 1706–1715.

Ju Z, Zhang H, Li X, et al. (2022) A survey on attack detection and resilience for connected and automated vehicles: from vehicle dynamics and control perspective. *IEEE Transactions on Intelligent Vehicles*: 1–24.

Kapoor N, Teel AR and Daoutidis P (1998) An anti-windup design for linear systems with input saturation. *Automatica* 34(5): 559–574.

Karafyllis I and Krstic M (2013) Stabilization of nonlinear delay systems using approximate predictors and high-gain observers. *Automatica* 49(12): 3623–3631.

Khalil HK and Grizzle JW (2002) *Nonlinear Systems*, Vol. 3. Upper Saddle River, NJ: Prentice hall.

Kosko B and Burgess JC (1998) *Neural Networks and Fuzzy Systems*.

Lagarias JC, Reeds JA, Wright MH, et al. (1998) Convergence properties of the nelder–mead simplex method in low dimensions. *SIAM Journal on Optimization* 9(1): 112–147.

Lee S, Joung S, Ha HG, et al. (2022) 3d image-guided robotic system for bone fracture reduction. *IEEE Robotics and Automation Letters* 7(2): 4353–4360.

Li M and Chen Y (2018) Robust adaptive sliding mode control for switched networked control systems with disturbance and faults. *IEEE Transactions on Industrial Informatics* 15(1): 193–204.

Ma M, Sun C and Chen X (2018) Deep coupling autoencoder for fault diagnosis with multimodal sensory data. *IEEE Transactions on Industrial Informatics* 14(3): 1137–1145.

Merlet JP (2006) *Parallel Robots*, Vol. 128. Springer Science & Business Media.

Minnoye A, Tajdari F, Doubrovski E, et al. (2022) Personalized product design through digital fabrication. In: International Design Engineering Technical Conferences & Computers and Information in Engineering Conference.

Navvabi H and Markazi A (2019) New afsmc method for nonlinear system with state-dependent uncertainty: application to hexapod robot position control. *Journal of Intelligent and Robotic Systems* 95(1): 61–75.

Nomura K, Yonezawa T, Takemura H, et al. (2016) Development of six-dof human ankle motion control device using stewart platform structure for fall prevention. *Journal of Robotics and Mechatronics* 28(5): 654–663.

Orekhov AL, Black CB, Till J, et al. (2016) Analysis and validation of a teleoperated surgical parallel continuum manipulator. *IEEE Robotics and Automation Letters* 1(2): 828–835.

Qi X and Cai ZJ (2021) Cooperative pursuit control for multiple underactuated underwater vehicles with time delay in three-dimensional space. *Robotica* 39(6): 1101–1115.

Robotis (2019) *Mx - 64 servo motor*. URL: http://emanual.robotis.com/docs/en/dxl/mx/mx-64-2/

Saeedi-Hosseiny MS, Alruwaili F, McMillan S, et al. (2021) A surgical robotic system for long-bone fracture alignment: prototyping and cadaver study. *IEEE Transactions on Medical Robotics and Bionics* 4: 172–182.

Shoham M, Burman M, Zehavi E, et al. (2003) Bone-mounted miniature robot for surgical procedures: concept and clinical applications. *IEEE Transactions on Robotics and Automation* 19(5): 893–901.

Slotine JJE, Li W, et al. (1991) *Applied Nonlinear Control*. Vol. 199. Englewood Cliffs, NJ: Prentice hall.

Sun Y, Jiang Z, Qi X, et al. (2018) Robot-assisted decompressive laminectomy planning based on 3d medical image. *IEEE Access* 6: 22557–22569.

Szufnarowski F (2013) Stewart platform with fixed rotary actuators: a low cost design study. *Advances in medical Robotics(4)*.

Taghirad HD (2013) *Parallel Robots: Mechanics and Control*. Boca Raton: CRC press.

Tajdari F and Toulkani NE (2021) Implementation and intelligent gain tuning feedback–based optimal torque control of a rotary parallel robot. *Journal of Vibration and Control* 28: 10775463211019177.

Tajdari F, Eijck C, Kwa F, et al. (2022a) Optimal position of cameras design in a 4D foot scanner. In: International Design Engineering Technical Conferences and Computers and Information in Engineering Conference, Vol. 2022, pp. 1–9.

Tajdari F, Huysmans T, Yang Y, et al. (2022b) Feature preserving non-rigid iterative weighted closest point and semi-curvature registration. *IEEE Transactions on Image Processing* 31: 1841–1856.

Tajdari F, Kabganian M, Khodabakhshi E, et al. (2017a) Design, implementation and control of a two-link fully-actuated robot capable of online identification of unknown dynamical parameters using adaptive sliding mode controller. In: 2017 Artificial Intelligence and Robotics (IRANOPEN), Azvin, Iran, 09–09 April 2017. IEEE, pp. 91–96.

Tajdari F, Kabganian M, Rad NF, et al. (2017b) Robust control of a 3-dof parallel cable robot using an adaptive neuro-fuzzy inference system. In: 2017 Artificial Intelligence and Robotics (IRANOPEN), Azvin, Iran, 09–09 April 2017. IEEE, pp. 97–101.

Tajdari F and Roncoli C (2021) Adaptive traffic control at motorway bottlenecks with time-varying fundamental diagram. *IFAC-PapersOnLine* 54(2): 271–277.

Tajdari F and Roncoli C (2022) Online set-point estimation for feedback-based traffic control applications. arXiv preprint arXiv:2207.13467.

Tajdari F, Roncoli C, Bekiaris-Liberis N, et al. (2019) Integrated ramp metering and lane-changing feedback control at motorway bottlenecks. In: 2019 18th European Control Conference (ECC), Naples, Italy, 25–28 June 2019. IEEE, pp. 3179–3184.

Tajdari F, Roncoli C and Papageorgiou M (2022c) Feedback-based ramp metering and lane-changing control with connected and automated vehicles. *IEEE Transactions on Intelligent Transportation Systems* 23(2): 939–951. DOI: 10.1109/TITS.2020.3018873.

Tajdari F, Tajdari M and Rezaei A (2021) Discrete time delay feedback control of stewart platform with intelligent optimizer weight tuner. In: 2021 IEEE International Conference on Robotics and Automation (ICRA), Xi'an, China, 30 May–05 June 2021. IEEE, pp. 12701–12707.

Tajdari F, Toulkani NE and Zhilakzadeh N (2020a) Intelligent optimal feed-back torque control of a 6dof surgical rotary robot. In: 2020 11th Power Electronics, Drive Systems, and Technologies Conference (PEDSTC), Tehran, Iran, 04–06 February 2020: IEEE, pp. 1–6.

Tajdari F, Toulkani NE and Zhilakzadeh N (2020b) Semi-real evaluation, and adaptive control of a 6dof surgical robot. In: 2020 11th Power Electronics, Drive Systems, and Technologies Conference (PEDSTC), Tehran, Iran, 04–06 February 2020: IEEE, pp. 1–6.

Tourajizadeh H, Yousefzadeh M and Tajik A (2016) Closed loop optimal control of a stewart platform using an optimal feedback linearization method. *International Journal of Advanced Robotic Systems* 13(3): 134.

Van Nguyen T and Ha C (2018) RBF neural network adaptive sliding mode control of rotary stewart platform. In: *International Conference on Intelligent Computing*. Springer, pp. 149–162.

Velasco JP, Calvo IG, Barambones OC, et al. (2020) Experimental validation of a sliding mode control for a stewart platform used in aerospace inspection applications. *Mathematics* 8(11): 2051.

Wang Y, Chen B and Wu H (2018a) Joint space tracking control of underwater vehicle-manipulator systems using continuous nonsingular fast terminal sliding mode. *Proceedings of the Institution of Mechanical Engineers - Part M: Journal of Engineering for the Maritime Environment* 232(4): 448–458.

Wang Y, Yan F, Chen J, et al. (2018b) A new adaptive time-delay control scheme for cable-driven manipulators. *IEEE Transactions on Industrial Informatics* 15(6): 3469–3481.

Williams RL and Lawrence DA (2007) *Linear State-Space Control Systems*. Hoboken, NJ: Wiley Online Library.

Xu X and Xu S (2022) Event-triggered adaptive neural tracking control of flexible-joint robot systems with input saturation. *IEEE Access* 10: 43367–43375.

Yang X, Wu H, Chen B, et al. (2019) Dynamic modeling and decoupled control of a flexible stewart platform for vibration isolation. *Journal of Sound and Vibration* 439: 398–412.

Zhu C, Chen J and Zhang H (2022) Attitude control for quadrotors under unknown disturbances using triple-step method and nonlinear integral sliding mode. *IEEE Transactions on Industrial Electronics*. 1–9.